INTERNAL STRESS PLASTICITY DUE TO CHEMICAL STRESSES

C. SCHUH and D. C. DUNAND†

Department of Materials Science and Engineering, Northwestern University, 2225 N. Campus Drive, Evanston, IL 60208, USA

Abstract—Internal stress plasticity occurs when a small external stress biases internal mismatch strains produced by, e.g., phase transformation or thermal expansion mismatch. At small applied stresses, this deformation mechanism is characterized by a deformation rate which is proportional to the applied stress and is higher than for conventional creep mechanisms. In this work, we demonstrate the operation of internal stress plasticity due to internal chemical stresses produced by chemical composition gradients. We subject specimens of β-phase Ti-6Al-4V to cyclic charging/discharging with hydrogen (by cyclic exposure of specimens to gaseous H_2), under a small external tensile stress. As expected for internal stress plasticity, the average strain rate during chemical cycles at 1030°C is larger than for creep at constant composition (hydrogen-free or -saturated), and a linear stress dependence is observed at small applied stresses. Additionally, we present an analytical model which couples elastic and creep deformation with a transient diffusion problem, wherein the diffusant species induces swelling of the host lattice. Without the use of any adjustable parameters, the model accurately predicts both the observed strain evolution during hydrogen cycling of Ti-6Al-4V and the measured stress dependence of the deformation. © 2001 Acta Materialia Inc. Published by Elsevier Science Ltd. All rights reserved.

Keywords: Internal stress plasticity

1. INTRODUCTION

The phenomenon of internal stress plasticity is observed in materials which are externally stressed while simultaneously experiencing internal mismatch strains [1]. The external stress biases these mismatch strains, which develop (by a plastic deformation mechanism such as yield or creep) preferentially in the direction of the external stress. Internal stress plasticity is commonly observed during thermal cycling, where internal mismatch strains develop due to (i) thermal expansion mismatch between coexisting phases, as in metal-matrix composites (e.g., in Al/SiC [2–5], Al/Be [6], or Al/Al₃Ni [7]), (ii) thermal expansion mismatch between adjacent grains in an anisotropic solid (e.g., Zn [8–10] or U [10, 11]), or (iii) density mismatch between polymorphic phases during a solid/solid phase transformation (e.g., in Fe and Fe-alloys [12–15], Ti and Ti-alloys [12, 16–19], and other polymorphic materials [12, 20, 21]). Recently,

some investigators have demonstrated internal stress plasticity during pressure cycling, at constant temperature, due to (i) compressibility mismatch between phases in a composite (in Al/SiC, in uniaxial tension or during powder compaction [22, 23]), and (ii) pressure-induced allotropic phase transformation (in H_2O ice [24]).

In all of the above cases, internal stress plasticity is characterized by two main features. First, at low levels of applied stress, the global deformation obeys a linear flow law, where the average strain rate during cycling is proportional to the applied stress. This linearity is noteworthy because, under isothermal (and isobaric) conditions, these materials typically exhibit a deformation power-law with a higher stress exponent, $n = 3-8$. Second, because of its low stress exponent, internal stress plasticity occurs at a faster rate than creep in the absence of internal stresses at low applied stresses. The combination of high flow stability and rapid deformation at low stresses makes internal stress plasticity of interest in shape forming; after multiple thermal or pressure cycles, this mechanism often leads to very large tensile elongation (>100%) and is thus often described as *internal stress superplasticity* [1].

---

† To whom all correspondence should be addressed. Tel.: +1-847-491-5370; fax: +1-847-467-6573.
E-mail address: dunand@northwestern.edu (D. C. Dunand)

In addition to thermal and pressure cycling, there is a possibility of inducing internal stress plasticity by cycling the chemical composition of a material while subjecting it to an external stress. Indeed, recent experiments by Frary *et al.* [25] and by Zwigl and Dunand [26, 27] have demonstrated that cycles of hydrogen alloying/dealloying can induce internal stress plasticity in titanium. Both of these investigations involved cyclic alloying of titanium with hydrogen, which was introduced as H_2 in the test atmosphere and removed by vacuum annealing. However, most of the experiments in these studies involved the α/β phase transformation of titanium, which is triggered at a critical concentration of hydrogen.

During chemical cycles such as those described above, the absorption of a diffusant leads to a swelling expansion of the crystal lattice. Because of concentration gradients of the diffusing species, a swelling gradient is established, leading to so-called chemical stresses [28]. At low temperatures, these stresses are accommodated elastically, as analyzed in Refs. [28–32]. At elevated temperatures, these internal chemical stresses may be accommodated by creep, leading to internal stress plasticity. Although the experiments described above [25–27] have examined deformation during chemical cycling, they have not presented evidence for internal stress plasticity due solely to mismatch from chemical swelling.

In the present work, we measure the tensile deformation of the engineering alloy Ti-6Al-4V at 1030°C (in the β phase) under conditions of cyclic charging/discharging with hydrogen. We demonstrate that chemical stress gradients, without a phase transformation, are sufficient to produce internal stress plasticity. Additionally, we present an analytical model that considers the superposition of internal chemical stress with an external uniaxial stress, and compare the model predictions to the present experiments.

2. EXPERIMENTAL PROCEDURES

Powder metallurgy Ti-6Al-4V billets (from Dynamet Technology, Burlington, MA) were machined into tensile specimens of 20 mm gauge length and 5 mm gauge diameter. Tensile deformation experiments were conducted in a custom creep apparatus described in Ref. [20], at a constant temperature of 1030°C, monitored by a type-K thermocouple in contact with the specimen gauge. Deformation of the specimen was measured with a linear voltage-displacement transducer at the cold end of the load train. Two different gas mixtures were used for the test atmosphere during the experiments; high-purity argon (99.999%) and a mixture of high-purity argon with 3.66% H_2. At atmospheric pressure, these two atmospheres correspond to hydrogen partial pressures of $P_{H2} = 0.0$ and 3.8 kPa, respectively. The gas flow rate was maintained at 1.3 l/min, ensuring that the volume of

gas in the test apparatus was exchanged about every 25 s. Gas was introduced into the apparatus through a sprayer to insure that the flow of gas was turbulent around the specimen, preventing concentration gradients in the test atmosphere.

Limited isothermal creep data was collected at 1030°C at various small stresses (0.5–5 MPa), and in both test atmospheres (Ar and Ar/H_2). Tensile deformation was also investigated at 1030°C during cycling of the test atmosphere between $P_{H2} = 0.0$ and 3.8 kPa. Two types of cycles were used, with periods of 24 and 30 min. Thus, during a single cycle, specimens were exposed to 12 or 15 min of the Ar/H_2 mixture, followed by an equal exposure to the high-purity Ar atmosphere. In every case, at least 3 consecutive chemical cycles were performed to insure a dynamic steady-state, and to verify reproducibility of the specimen length changes during chemical cycling.

3. RESULTS

At the test temperature (1030°C), Ti-6Al-4V is single phase, with Al and V in solid solution within BCC β-Ti [33]. Furthermore, the introduction of hydrogen to the β-Ti phase of Ti-6Al-4V does not cause a phase transformation [34, 35]. Thus, for all of the experimental conditions examined in this work, the material was in the β-phase field. The microstructure both before and after the high-temperature experiments was found to consist of large (100–400 μm) prior-β grains.

The isothermal creep data at 1030°C are shown in Fig. 1, with the uniaxial strain rate $\dot{\varepsilon}$ plotted against the applied tensile stress σ. The strain rate data exhibits a power-law stress dependence:
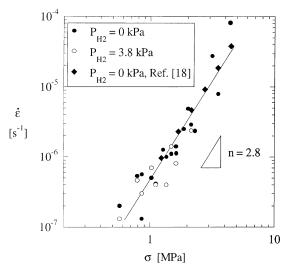
$$\dot{\varepsilon} = K \cdot \sigma^n \qquad (1)$$

Fig. 1. Isothermal creep rate of Ti-6Al-4V as a function of the uniaxial tensile stress at 1030°C, in a high-purity argon atmosphere as well as the Ar/H_2 mixture.

with a stress exponent n close to three and with some scatter between different specimens. The test atmosphere (Ar or Ar/H$_2$) did not appreciably affect the creep behavior of the alloy, as shown in pure Ti for these low strain rates and hydrogen pressures [36]. All of the data can be fitted to equation (1) with values of $K = 4.8 \cdot 10^{-7}$ MPa$^{-2.8}$ and $n = 2.8$. These values are very close to those obtained in our previous work [18] on hydrogen-free Ti-6Al-4V at the same temperature ($K = 4.7 \cdot 10^{-7}$ MPa$^{-2.8}$ and $n = 2.8$), and are in broad agreement with data from the literature for deformation of hydrogen-free Ti-6Al-4V at similar temperatures (1000–1100°C) and higher stresses (6.4–160 MPa) [37, 38].

During chemical cycling, the average deformation rates were larger than for isochoral creep (i.e., creep at constant composition) in either Ar or Ar/H$_2$. Typical results are shown in Fig. 2 for the 24 min cycles, where the true strain of the specimen gauge is plotted as a function of time during the chemical cycles. Similar curves were obtained for the 30 min cycles. During exposure to gaseous H$_2$, the specimen absorbs atomic hydrogen and the crystal lattice swells, giving rise to a transient increase in specimen length. On the second half of the cycle, during annealing in pure Ar, the dissolved hydrogen diffuses to the specimen surface and escapes into the hydrogen-free atmosphere, causing a contraction of the specimen gauge. Near the end of each half-cycle, the diffusion of hydrogen into or out of the specimen is complete, and the specimen deforms only by steady-state creep. For comparison with the cycling data, the steady-state isochoral creep predicted by equation (1) is also shown as dashed lines in Fig. 2. The experimental deformation rates measured near the end of the charging or discharging half-cycles are in good agreement with these expected creep rates. Finally, we note that in all cases, the strain history during chemical cycling was identical, within experimental error, for each consecutive chemical cycle at the same stress.

The enhanced deformation during chemical cycling is also shown in Fig. 3, where the strain increment $\Delta\varepsilon$ developed after each full chemical cycle is plotted as a function of the applied tensile stress σ. The amount of strain expected due to creep (following equation (1)) at a constant composition (H-free or H-saturated) is shown for comparison. Whereas isochoral creep strain developed over a fixed duration is expected to follow a power-law relationship with a stress exponent of about 2.8 (Fig. 1), the deformation during chemical cycling is characterized by a stress exponent near unity, and is significantly more rapid than the expected power-law creep.

Finally, we note that the deformation during chemical cycling was approximately equal for the 24- and 30-min chemical cycles, indicating that the specimens were completely charged with hydrogen within 12 min. Since deformation during chemical cycling is fast compared to creep without cycling, the additional 6 min of creep (30- compared to 24-min cycles) do not appreciably increase the average rate of deformation during cycling.

4. DISCUSSION

The observed stress exponent of unity (Fig. 3) and the enhanced rate of deformation observed during chemical cycling (Figs 2 and 3) are the defining characteristics of internal stress plasticity, and indicate that the internal stresses due to the gradient in lattice swelling are sufficient to activate this deformation mechanism. To our knowledge, this is the first direct observation of internal stress plasticity due
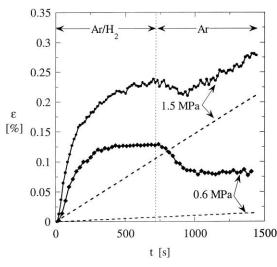
Fig. 2. True strain history of Ti-6Al-4V during 24-min chemical cycles, at two different applied stresses and 1030°C. Shown for comparison is the expected creep history for a specimen with constant composition deforming in pure Ar or Ar/H$_2$ mixture (dashed lines).
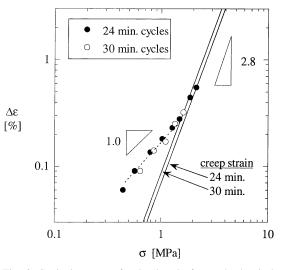
Fig. 3. Strain increment $\Delta\varepsilon$ developed after each chemical cycle, plotted as a function of the applied tensile stress σ. The strain expected by creep without chemical cycling is also shown for comparison.

solely to swelling mismatch during a process of cyclic alloying. Our results are also in agreement with some trends observed in recent studies in the Ti-H system during cyclic alloying, as described in the following.

First, in a single experiment at 1000°C, Frary *et al.* [25] showed that one cycle of hydrogen addition to, and removal from, β-titanium, without any phase transformation and in the absence of any external stress, caused plastic deformation by ratchetting. They measured a plastic axial shrinkage of 0.07% in a long cylinder of titanium, in which hydrogen diffusion was predominantly radial. However, these authors considered only deformation without external stress (ratchetting), and thus could not establish the linear flow law observed in the present work for Ti-6Al-4V (Fig. 3). Second, Zwigl and Dunand [26, 27] have investigated uniaxial deformation during cyclic charging of unalloyed titanium with hydrogen, under conditions where the chemical cycles induced the titanium α/β allotropic transformation. They found a linear relationship between $\Delta\varepsilon$ and σ, but noted that the internal stress generation was due to a complex superposition of chemical stresses from lattice swelling and transformation stresses due to the mismatch in density between α- and β-Ti. The present results are in line with these studies, and further demonstrate that swelling mismatch due to a hydrogen concentration gradient can produce sufficient internal stresses to induce internal stress plasticity, without the necessity of a phase transformation.

4.1. Deformation during chemical half-cycles

During a chemical cycle, the observed deformation is composed of several additive contributions. First, the swelling of the crystal lattice due to hydrogen charging ($\Delta\varepsilon_{s,c}$) is fully recovered upon discharging ($\Delta\varepsilon_{s,d} = -\Delta\varepsilon_{s,c}$). Second, the plastic deformation due to internal stress plasticity, $\Delta\varepsilon_{isp}$, is not reversible and accumulates on each half of the chemical cycle; thus, there are two half-cycle contributions to the deformation, $\Delta\varepsilon_{isp,c}$ on charging, and $\Delta\varepsilon_{isp,d}$ on discharging. Finally, it is possible to induce permanent plastic deformation during chemical cycling in the absence of external stresses. This strain ratchetting, which was demonstrated by Frary *et al.* [25] during chemical cycles in the Ti-H system, is usually considered independent of the applied stress [39], and represents a third contribution to deformation ($\Delta\varepsilon_{r,c}$ on charging and $\Delta\varepsilon_{r,d}$ on discharging). At low stresses, creep is slow compared to internal stress plasticity (Fig. 3), and may be neglected as a contributor to deformation. Thus, on the charging or discharging half-cycles, the total strain is given by the linear addition of these three contributions:

$$\Delta\varepsilon_c = \Delta\varepsilon_{s,c} + \Delta\varepsilon_{r,c} + \Delta\varepsilon_{isp,c} \qquad (2a)$$

$$\Delta\varepsilon_d = \Delta\varepsilon_{s,d} + \Delta\varepsilon_{r,d} + \Delta\varepsilon_{isp,d} \qquad (2b)$$

Although the chemical swelling strains $\Delta\varepsilon_s$ are equal and opposite on the two halves of the chemical cycle, the amount of deformation due to internal stress plasticity $\Delta\varepsilon_{isp}$ and ratchetting $\Delta\varepsilon_r$ may be different for the charging and discharging half cycles. At low stresses, internal stress plasticity occurs with a linear stress dependence, $\Delta\varepsilon_{isp} = (d\Delta\varepsilon/d\sigma)\cdot\sigma$, where $d\Delta\varepsilon/d\sigma$ is the slope of the linear relationship, and is dependent upon the internal strain state and the deformation characteristics of the material (see, e.g., Refs [12, 40]). Because the swelling and ratchetting strain contributions are assumed independent of the applied external stress, equation (2) can be rewritten:

$$\Delta\varepsilon_c = \Delta\varepsilon_{s,c} + \Delta\varepsilon_{r,c} + \frac{d\Delta\varepsilon_{isp,c}}{d\sigma}\cdot\sigma \qquad (3a)$$

$$\Delta\varepsilon_d = \Delta\varepsilon_{s,d} + \Delta\varepsilon_{r,d} + \frac{d\Delta\varepsilon_{isp,d}}{d\sigma}\cdot\sigma \qquad (3b)$$

According to equation (3), plotting $\Delta\varepsilon_c$ or $\Delta\varepsilon_d$ against the applied tensile stress should give a linear relationship, the slope of which is the deformation due to internal stress plasticity during each half-cycle. Thus, the amount of deformation during both hydrogen charging and discharging can be revealed in this manner, as done previously for thermal cycling experiments [18, 20].

Figure 4 shows this relationship, plotted for hydrogen cycles of both 24- and 30-min duration. Since internal stress superplasticity is only expected to be linear at small applied stresses [1], only data points for $\sigma < 1.5$ MPa are shown. As expected, the relationship between $\Delta\varepsilon$ and σ is linear, for both charging
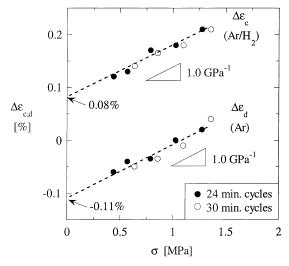

Fig. 4. Measured strain increment after each chemical half-cycle, as a function of the applied stress, indicating equal contributions to deformation for the charging and discharging portions of a single cycle, and the lattice swelling extrapolation to the origin.

and discharging half-cycles. Furthermore, the slopes of these two lines are found to be equal, $d\Delta\varepsilon_c/d\sigma = d\Delta\varepsilon_d/d\sigma = 1.0$ GPa^{-1}; internal stress plasticity thus is found to occur equally on the charging and discharging half-cycles. The total superplastic slope, $d\Delta\varepsilon/d\sigma = 2.0$ GPa^{-1}, found by adding the two half-cycle contributions, is in the range of reported values obtained for thermal cycling through the α/β phase transformation range of Ti-6Al-4V (from 0.5 to 2.5 GPa^{-1}, depending on the thermal cycle shape and size [18]). Although the specimens in this study never experienced more than about 10% elongation, our observations of internal stress plasticity suggest that, if exposed to many chemical cycles, Ti-6Al-4V could exhibit internal stress superplasticity (strains greater than 100%).

4.2. Chemical swelling and strain ratchetting

According to equation (3), the intercepts on Fig. 4 provide information about the swelling and ratchetting strains during chemical cycling. First, without applied stress, the contribution of internal stress plasticity is nil, so the net deformation after a complete chemical cycle, $\Delta\varepsilon_c + \Delta\varepsilon_d = -0.03\%$ is due solely to chemical ratchetting. Both the sign and the magnitude of this value agree with the value reported by Frary *et al.* [25] for hydrogen cycling of pure Ti in the β-field at 1000°C ($\Delta\varepsilon_r \approx -0.07\%$), although those authors used a somewhat larger partial pressure of H$_2$ (P$_{H2} = 5.1$ vs. 3.8 kPa in the present study) and a longer cycle time (55 vs. 24 or 30 min in the present work).

The total ratchetting strain ($\Delta\varepsilon_r = -0.03\%$) may evolve completely during charging, completely during discharging, or may be a sum of two independent contributions from the charging and discharging half-cycles. Thus, it is impossible to accurately determine the swelling strain $\Delta\varepsilon_s$ ($= \Delta\varepsilon_{s,c} = -\Delta\varepsilon_{s,d}$) from equation (3). However, based on equation (3) and the extrapolated intercepts in Fig. 4, we can conclude that the swelling strain must be between the values of $\Delta\varepsilon_s = 0.08$ and 0.11%. These two values correspond to the ratchetting strain developing entirely upon charging, and entirely upon discharging, respectively. In what follows, we consider the physics of chemical swelling, in order to verify that the above range of swelling strains is reasonable.

The diffusion of hydrogen into metals has been investigated by numerous authors (see, e.g., Refs. [41, 42] for reviews of the Ti-H system), and in almost every case, the linear strain $\Delta\varepsilon_s$ associated with lattice swelling due to dissolved hydrogen is found to be a linear function of the hydrogen concentration, c:

$$\Delta\varepsilon_s = \frac{1}{3}\frac{\Delta v}{\Omega}\cdot c \qquad (4)$$

where Δv is the partial molar volume of hydrogen, and Ω is the atomic volume of the metal into which

it diffuses. In the present case, Ti-6Al-4V in its solid-solution β-phase was exposed to gaseous hydrogen at a partial pressure of P$_{H2} = 3.8$ kPa. The equilibrium amount of absorbed hydrogen, c_{eq} is given, for pure β-Ti, by Sievert's law [42]:

$$\log_{10}(P_{H2}) = 2\cdot\log_{10}(c_{eq}) + 9.47 - \frac{4720}{T} \qquad (5)$$

where T is the absolute temperature and P$_{H2}$ is in Pa. At the test temperature (1030°C) and hydrogen partial-pressure used in the present study, equation (5) gives $c_{eq} = 7.3$ at% hydrogen. Thus, after complete charging, the swelling of the β-phase Ti-6Al-4V corresponds to a dissolved hydrogen concentration of 7.3 at%, if the solid solution elements (Al and V) have an insignificant effect on solubility and swelling. While the effect of these elements on the hydrogen solubility of β-Ti-6Al-4V is unclear, the addition of 6 wt% Al to α-Ti is known to reduce the hydrogen solubility by about a factor of two [43]. If this relationship is also true for β-Ti-6Al-4V, then the dissolved hydrogen concentration may be as low as 3.7 at%. Using these two possible values for c (7.3 or 3.7 at%), and taking the atomic volume of β-Ti-6Al-4V to be the same as β-Ti, $\Omega = 18.1$ Å^3 [44], as well as the measured upper- and lower-bound linear swelling strains ($\Delta\varepsilon = 0.08\%$ to 0.11%) from Fig. 4, equation (4) brackets the partial molar volume of hydrogen in β-Ti between $\Delta v = 0.60$ Å^3 and 1.6 Å^3. These values agree well with the broad range of values ($\Delta v = 0.75 - 1.81$ Å^3) found by previous authors for lattice swelling of various β-Ti alloys (but not Ti-6Al-4V) at various temperatures [45]. The direct measurement of Δv in Ti-6Al-4V by room-temperature diffraction techniques (e.g., Refs. [46, 47]) is complicated by significant internal mismatch strains between the coexisting α and β phases [47].

4.3. Modeling internal stress plasticity due to chemical stresses

As described in the Introduction, there are many possible mechanisms for internal stress plasticity, including thermal expansion mismatch, compressibility mismatch, and phase transformation mismatch. Accordingly, there have been many models proposed to predict the stress dependence of the deformation during thermal or pressure cycling [4, 12, 40, 48]. However, these models are often specific to the type of mismatch they consider, and several are dependent on microstructural geometry. None of the existing models is suitable to predict the deformation we observe during chemical cycling. Therefore, in this section we develop an analytical model to describe uniaxial deformation under the action of an external stress and internal chemical stresses, which arise due to lattice swelling upon the introduction of a diffusant. A thorough description of the coupled diffusion/deformation problem for arbitrary geo-

metries under multiaxial stress conditions would require elaborate finite-element type models. The approach taken here is considerably simpler and more versatile, but still incorporates the essential physical conditions of the problem. The three main assumptions we employ in the model are listed below:

1. We consider the uniaxial deformation of a very long (infinite) specimen of uniform cross section, under a constant applied stress σ_A in the long dimension. For the purposes of the calculations, the specimen cross-section is divided into N units of infinite length, as shown for an infinite cylinder in Fig. 5.
2. We assume that the stress state in the specimen is primarily uniaxial; transverse stresses are thus explicitly neglected in the subsequent mathematical developments. This simplified approach was selected for two reasons. First, this type of uniaxial model has often been employed to model, e.g., fiber-reinforced composites or coated fibers [49–55] during thermal excursions or uniaxial loading. Despite neglecting the complex triaxiality of true composite stress states, these models have proven to be reasonably accurate for most purposes, including conditions of elasticity, plasticity, and creep. Zhang *et al.* [56] have compared such a one-dimensional approximation to a more complex axisymmetric model for a long fiber embedded in a cylindrical matrix under conditions of
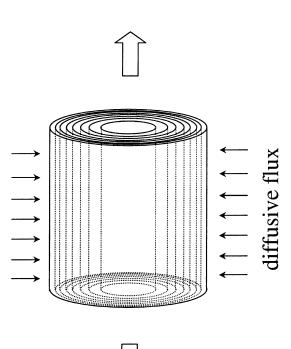
Fig. 5. Cylindrical geometry considered in the analytical model, assumed to be very long in the tensile axis, and divided into N concentric elements ($N = 8$ is shown here).

thermal cycling, and noted that there are many cases where the uniaxial model is a reasonable approximation for the multiaxial solution. Second, the uniaxial approximation is easy to implement and leads to a simple and useful result, but more importantly, it does not require that the cross-sectional geometry be specified. The details of the cross-sectional geometry are thus only important as regards the diffusion problem. In the present work we consider the specific case of a long cylinder (circular cross-section), but the uniaxial model allows for ready adaptation to any other cross-sectional geometry.
3. In the model, chemical stress gradients are produced upon introduction of a diffusant at the surface of the specimen. Because the specimen is very long in one dimension, chemical diffusion is taken to occur only in the plane perpendicular to the stress axis. Additionally, the applied stress is assumed small enough that it does not impact the diffusivity of the diffusant species. In the practical cases we will consider later, the stress range of interest is $\sigma_A < 5$ MPa, for which this assumption is reasonable.

In the following section, we first develop the mechanical aspects of the model, independently of the cross-sectional geometry. The diffusion problem is then treated separately in a later section.

4.3.1. Mechanics of deformation. Following the assumption of a purely uniaxial stress state, each of the N elements in the specimen has a stress σ_i and cross-sectional area A_i ($i = 1$ to N), and together the elements must obey an axial force balance:

$$\sum_{i=1}^{N} \sigma_i \cdot A_i = \sigma_A \cdot A \qquad (6)$$

where A is the total cross-sectional area of the specimen. In addition, to maintain strain compatibility, the strain ε_i must be equal in all of the elements:

$$\varepsilon_i = \varepsilon_{i-1}, \ (i = 2 \text{ to } N) \qquad (7)$$

We consider situations in which the material sustains plastic deformation by creep, where the creep strain rate, $\dot{\varepsilon}_i^c$, obeys a power-law in stress:

$$\dot{\varepsilon}_i^c = sign(\sigma_i) \cdot K_i \cdot |\sigma_i|^{n_i} \qquad (8)$$

where $sign(\sigma_i)$ denotes the sign of the stress (positive for tension or negative for compression), K_i is a temperature-dependent constant, and n_i is the power-law stress exponent. At any instant in time, the material can also sustain elastic strains which are given by Hooke's Law:

$$\varepsilon_i^e = \frac{\sigma_i}{E_i} \tag{9a}$$

If the Young's modulus, E, in each element is independent of time, then equation (9a) can be differentiated with respect to time as:

$$\dot{\varepsilon}_i^e = \frac{\dot{\sigma}_i}{E_i} \tag{9b}$$

The instantaneous strain rate in each element is thus composed of these two deformation contributions (elasticity and creep), and a third contribution due to chemical swelling, $\dot{\varepsilon}_i^s$:

$$\dot{\varepsilon}_i = \dot{\varepsilon}_i^c + \dot{\varepsilon}_i^e + \dot{\varepsilon}_i^s \tag{10}$$

The physical constitutive law describing chemical swelling will be discussed later; at present we proceed assuming that the value of $\dot{\varepsilon}_i^s$ can be calculated at any point in time in each element. Now, combining equations (7–10) gives $N-1$ similar equations:

$$\frac{\dot{\sigma}_{i-1}}{E_{i-1}} - \frac{\dot{\sigma}_i}{E_i} = \dot{\varepsilon}_i^s - \dot{\varepsilon}_{i-1}^s + sign(\sigma_i) \cdot K_i \cdot |\sigma_i|^{n_i} \tag{11}$$
$$- sign(\sigma_{i-1}) \cdot K_{i-1} \cdot |\sigma_{i-1}|^{n_{i-1}}, \quad (i = 2 \text{ to } N)$$

An additional equation is found by differentiating equation (6) with respect to time, assuming a constant applied stress:

$$\sum_{i=1}^{N} \dot{\sigma}_i \cdot A_i = 0 \tag{12}$$

The terms in equations (11) and (12) are composed of known materials parameters (E, K, and n), the area of each element, A_i, and the instantaneous stress state in the elements. If, at a given moment, all of these parameters are known, then equations (11) and (12) constitute a system of N equations, the N unknowns being the rates of stress change in the elements, $\dot{\sigma}_i$. These equations are conveniently expressed in matrix form, with equation (12) occupying the upper row:

$$\begin{bmatrix} A_1 & A_2 & A_3 & \dots & A_N \\ 1/E_1 & -1/E_2 & 0 & \dots & 0 \\ 0 & 1/E_2 & -1/E_3 & \dots & 0 \\ \vdots & \vdots & \vdots & \ddots & \vdots \\ 0 & 0 & 0 & 1/E_{N-1} & -1/E_N \end{bmatrix} \begin{bmatrix} \dot{\sigma}_1 \\ \dot{\sigma}_2 \\ \dot{\sigma}_3 \\ \vdots \\ \dot{\sigma}_N \end{bmatrix} = \begin{bmatrix} 0 \\ b_2 \\ b_3 \\ \vdots \\ b_N \end{bmatrix} \tag{13}$$

in which the terms on the right-hand side are given by:

$$b_i = \dot{\varepsilon}_i^s - \dot{\varepsilon}_{i-1}^s + sign(\sigma_i) \cdot K_i \cdot |\sigma_i|^{n_i} \tag{14}$$
$$- sign(\sigma_{i-1}) \cdot K_{i-1} \cdot |\sigma_{i-1}|^{n_{i-1}}, \quad (i = 2 \text{ to } N)$$

For the general case where the elements have different areas and different elastic moduli, equation (13) could be solved numerically using, e.g., Gaussian elimination or an iterative (Jacobian or Gauss–Seidel) method. However, a small concentration of diffusant species typically does not significantly change the elastic modulus; it is then reasonable to assume that the modulus is the same in each element, $E_i = E$ ($i = 1$ to N). Furthermore, if the elements are judiciously chosen such that they all have equal areas, the left-hand side of equation (13) can be written as a signed binary matrix:

$$\begin{bmatrix} 1 & 1 & 1 & \dots & 1 \\ 1 & -1 & 0 & \dots & 0 \\ 0 & 1 & -1 & \dots & 0 \\ \vdots & \vdots & \vdots & \ddots & \vdots \\ 0 & 0 & 0 & 1 & -1 \end{bmatrix} \begin{bmatrix} \dot{\sigma}_1 \\ \dot{\sigma}_2 \\ \dot{\sigma}_3 \\ \vdots \\ \dot{\sigma}_N \end{bmatrix} = E \cdot \begin{bmatrix} 0 \\ b_2 \\ b_3 \\ \vdots \\ b_N \end{bmatrix} \tag{15}$$

As shown in the appendix, the matrix on the left-hand side of equation (15) can be analytically reduced to the $N \times N$ identity matrix, and the system of N equations thereby solved in closed form (equation (A4)). The accuracy of the solution can be selected by varying the number of elements, N. For ease in numerical implementation, this solution (equation (A4)) can be rewritten in a recursive form, in which $\dot{\sigma}_1$ is computed directly as:

$$\dot{\sigma}_1 = \frac{E}{N} \cdot \sum_{j=2}^{N} b_j \cdot (N + 1 - j) \tag{16a}$$

and each subsequent term is computed by iterating the value of i and using:

$$\dot{\sigma}_i = \dot{\sigma}_1 - E \cdot \sum_{k=2}^{i} b_k, \quad (i = 2 \text{ to } N) \tag{16b}$$

or,

$$\dot{\sigma}_i = \dot{\sigma}_{i-1} - E \cdot b_i, \quad (i = 2 \text{ to } N) \tag{16c}$$

Simulation of the dynamic process of chemical cycling involves computing the stress state at many discrete moments during the cycle. At any instant in time, the stress state is fully known, and the rate of change of that stress state is calculated from equation (16). Then, a finite time step Δt is applied and the

stress state is updated using a forward-difference approximation:

$$\sigma_i^{t+\Delta t} = \sigma_i^i + \dot{\sigma}_i^t \cdot \Delta t, \quad (i = 1 \text{ to } N) \qquad (17)$$

The strain in each element is the same by assumption, so the instantaneous strain of the specimen is computed using the same running-integral approach:

$$\varepsilon_l^{t+\Delta t} = \varepsilon_l^t + \dot{\varepsilon}_l^t \cdot \Delta t \qquad (18)$$

where l is an arbitrarily chosen integer between 1 and N, and the instantaneous strain rate is calculated from equation (10). For the cases considered here, the strains experienced by the specimen are always quite small (usually less than 1% and always less than 3.5%); the lateral contraction of the elements can thus be reasonably neglected with respect to the diffusion problem described below.

4.3.2. Diffusion and chemical strains. Knowing the creep and elastic behavior of the material to be modeled, the above mechanics model is lacking only information regarding the chemical strain evolution during chemical cycling. As described earlier, the chemical swelling strain is simply proportional to the local concentration of hydrogen, with a proportionality constant $F \equiv \Delta v/3 \cdot \Omega$ (equation 4). Thus, the chemical strain is a simple function of the local concentration of diffusant, and can be calculated from an appropriate solution to Fick's second law of diffusion:

$$\frac{\partial c}{\partial t} = D \cdot \nabla^2 c \qquad (19)$$

where the diffusivity D is assumed concentration-independent. The boundary conditions on equation (19) are described by the conditions of the chemical cycling. On the charging half-cycle, the specimen is taken to be initially at a uniform concentration $c_o = 0$, and exposed to a constant surface concentration $c_s = c_{eq}$, where c_{eq} is the equilibrium concentration of the diffusant species at the temperature and pressure of the experiment. On the discharging half cycle, the specimen is initially at $c_o = c_{eq}$, and diffusion proceeds toward the surface, where the concentration is prescribed as $c_s = 0$. As described in Ref. [25], more complex boundary conditions can be considered, but we limit ourselves to the perfect square chemical cycle in the present work.

For the long cylinder geometry, all diffusion is assumed to occur radially, normal to the stress axis of the specimen. With the prescribed conditions for either charging or discharging, the appropriate solution to equation (19) is [57]:

$$c = (c_o - c_s) \cdot \left[1 - \frac{2}{a} \cdot \sum_{m=1}^{\infty} \frac{J_o(r \cdot \alpha_m)}{(a \cdot \alpha_m)} \cdot \frac{1}{\alpha_m} \right. $$
$$\left. \cdot \exp(-D \cdot \alpha_m^2 \cdot t) \right] + c_o \qquad (20)$$

where a is the cylinder radius, r is the radial coordinate, J_y is the Bessel function of the first kind of order y, and α_m are the positive roots of $J_0(a \cdot \alpha_m) = 0$.

As described previously, the mechanical model requires that the elements comprising the cylinder all have equal cross-sectional area. The most convenient division is to select $N-1$ concentric cylindrical shells, surrounding a solid cylindrical inner element, such that all of the elements have equal areas (Fig. 5). We take the first element ($i = 1$) to be at the surface of the cylinder, and the last element ($i = N$) to be the solid cylindrical core. Then we can derive a simple recursive relationship to determine the inner radius of each element, r_i^{inner}, which is equal to the outer radius of the subsequent element, $r_i^{inner} = r_{i+1}^{outer}$ ($i = 1$ to $N-1$). The first element is bounded by $r_1^{outer} = a$ and:

$$r_1^{inner} = a \cdot \sqrt{\frac{N-1}{N}} \qquad (21a)$$

and the subsequent element boundaries are found from:

$$r_i^{inner} = \sqrt{\frac{N \cdot (r_i^{outer})^2 - a^2}{N}}, \quad (i = 2 \text{ to } N) \quad (21b)$$

The average concentration in each element can now be determined using:

$$\bar{c}_i = \frac{2}{(r_i^{outer})^2 - (r_i^{inner})^2} \cdot \int_{r_i^{inner}}^{r_i^{outer}} c \cdot r \cdot dr \qquad (22)$$

and, finally, the rate of chemical strain evolution is determined by combining equations (20), (22) and (4), and differentiating with respect to time:

$$\dot{\varepsilon}_i^s = \frac{c_o - c_s}{(r_i^{outer})^2 - (r_i^{inner})^2} \cdot$$
$$\frac{4}{a} \cdot D \cdot F \cdot \sum_{m=1}^{\infty} \exp(-D \cdot \alpha_m^2 \cdot t) \cdot \qquad (23)$$
$$\frac{r_i^{outer} \cdot J_1(r_i^{outer} \cdot \alpha_m) - r_i^{inner} \cdot J_1(r_i^{inner} \cdot \alpha_m)}{J_1(a \cdot \alpha_m)}$$

4.3.3. Comparison with experiment. The model detailed in the previous sections allows the instantaneous stress and strain state in the specimen to be

calculated by stepping sequentially through time. At each time step, the chemical swelling rates (equation (23)) are input directly into equations (14) and (16), from which the instantaneous rate of stress change is computed in each element. The stress state, which must be known, is then updated with equation (17); in this formulation, the constant applied stress is introduced as an initial condition; at $t = 0$, $\sigma_i = \sigma_A$, for $i = 1$ to N.

As with any implicit finite-difference method, equations (17) and (18) are only valid for sufficiently small time steps; larger time steps lead to numerical instability. In particular, the early moments of each chemical half-cycle require extremely small time steps ($\sim 10^{-4}$–10^{-5} s for the conditions used in the subsequent examples). Additionally, the summation in equation (23) is slowly convergent at short times, so a large number of terms (we use 250) need to be computed to insure a reasonably accurate depiction of diffusion. Further details of the computational procedures are available in Ref. [58].

In applying this model to the present experiments, we employ a cylindrical geometry with a radius of $a = 2.5$ mm. During the experiments, this radius decreased somewhat (at most ~9%) due to plastic elongation of the specimens, but this contraction was found to produce no significant variation in the predictions of the model. In the model, $N = 100$ concentric annuli of equal cross-sectional area are defined, and the stress and strain state in each is tracked during a 24-min chemical cycle. The first half of the cycle involves diffusion with a fixed hydrogen concentration at the surface of $c_{eq} = 7.3$ at% (calculated earlier), and the second half-cycle involves a fixed surface concentration of $c = 0$ at%. The shear modulus of β-Ti at 1030°C is $G = 16$ GPa [44], from which the Young's modulus $E = 44$ GPa is calculated using $E = 2 \cdot G \cdot (1 + v)$, where the Poisson's ratio of β-Ti is taken as $v = 0.36$ [59]. The creep behavior of Ti-6Al-4V at 1030°C is described by equation (1), using the parameters determined experimentally ($K = 4.8 \cdot 10^{-7}$ MPa$^{-2.8}$ s^{-1} and $n = 2.8$, Fig. 1). As described in the previous section, the chemical swelling of the specimen occurs linearly in concentration, to a maximum concentration of $c_{eq} = 7.3$ at%. Since the experiments in this work could not unambiguously determine the swelling strain, $\Delta \varepsilon_s$, we examine the full range of possible values $\Delta \varepsilon_s = 0.08$–$0.11\%$ by using both the upper- and lower-bounds in the model. These bounds correspond to a range for the swelling constant $F = 0.11$–0.15 (defined as $\Delta \varepsilon_s/c_{eq}$). Finally, the diffusivity of atomic hydrogen in various β-Ti alloys (but not Ti-6Al-4V) has been reviewed by Christ et al. [60], and spans a broad range ($5 \cdot 10^{-6}$–$3 \cdot 10^{-4}$ cm^2/s) at 1030°C; we take an average value, $D = 7.5 \cdot 10^{-5}$ cm^2/s.

This model, with the input parameters described above, requires no additional adjustable parameters, and fully includes the effects of swelling, internal stress plasticity, and creep. Therefore, the predictions

of the model can be directly compared with the experimental data, without the need to separate these contributions from one another. Of particular interest is the strain increment evolved after a complete chemical cycle, $\Delta \varepsilon$. In Fig. 6, the experimental values of $\Delta \varepsilon$ from Fig. 3 are plotted against the applied stress, on linear axes. At low stresses the data fall on a line, with a deviation to a larger stress-dependence as the stress is increased. Shown for comparison are the predictions of the analytical model, using both the upper- and lower-bound values for the swelling strain, $\Delta \varepsilon_s$. Clearly, the predictions of the model are not strongly affected by the allowable variations in the swelling strain. Additionally, the model predictions are in excellent agreement with the experimental data over the full range of investigated stresses, both at low stresses, where the model and data exhibit the linear $\Delta \varepsilon$ vs. σ relationship expected for internal-stress plasticity, and at higher stresses, where the data and model both exhibit a smooth divergence to larger strain increments. This divergence is also typical for internal-stress plasticity by thermal cycling [10, 18, 40, 61]; when the external stress is very large compared to the internal stresses, deformation occurs primarily due to the external stress, according to the typical deformation power-law of the material.

In addition to the net deformation after a complete chemical cycle, the model is also capable of predicting the complete strain history during a hydrogen cycle. In Fig. 7, the predicted evolution of strain is shown for four different applied stresses, and compared with experimental data. For this purpose, the upper-bound swelling strain ($\Delta \varepsilon_s = 0.11\%$) presented a better agreement with the data and most of the model output in Fig. 7 thus uses this value; an example of the model output with $\Delta \varepsilon_s = 0.08\%$ is also shown for a single stress level. The model predicts
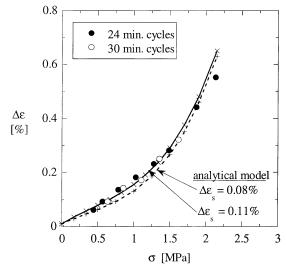
Fig. 6. Strain increment after each complete chemical cycle as a function of the applied tensile stress (from Fig. 3), compared with the predictions of the analytical model.
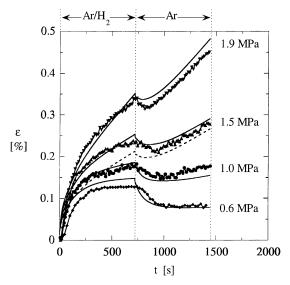
Fig. 7. Strain evolution during a single 24-min chemical cycle, experimental data (points) compared with the model predictions (lines), using the upper-bound swelling strain, $\Delta\varepsilon_s = 0.11\%$ (solid lines), or the lower-bound value, $\Delta\varepsilon_s = 0.08\%$ (dashed line).
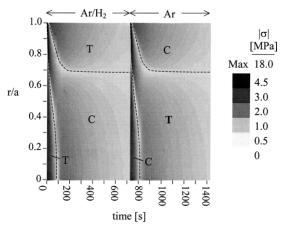

Fig. 8. Map of the longitudinal stress state during chemical cycling of Ti-6Al-4V, as predicted by the analytical model; regions in tension and compression are denoted by T and C, respectively, and dotted lines show the contours of $\sigma = 0$.

the general shape of the curves with accuracy, including the rate of swelling expansion, the steady-state deformation observed after the completion of hydrogen charging or discharging, and the total strain developed at the end of the cycle (Fig. 6).

In Figs 6 and 7, the small disagreement between the model and the experiments is probably due to several factors, including uncertainty in the hydrogen diffusivity and creep parameters, neglecting the kinetics of hydrogen sorption and desorption from the specimen surface, and the assumption of a simple uniaxial stress state. However, the model predicts the average strain rate during thermal cycling to within about 15% over the stresses investigated. We thus believe that a more complex modeling approach would only achieve marginal improvements in predictive power, and this simplified approach captures the essential physics of chemical cycling deformation.

4.4. Internal stress during chemical cycles

Because the model used here tracks the stress state in each element of the specimen through the chemical cycle, it can give a quantitative picture of the internal stress distribution due to chemical swelling gradients. Figure 8 shows a map of the internal stress state during a modeled cycle with $\sigma = 0$ and $\Delta\varepsilon_s = 0.11\%$ (i.e., the chemical stress state), at all points in the cylinder (from the center, $r/a = 0$, to the outer surface, $r/a = 1$), with stresses ranging from 0 MPa (white) to 18 MPa (black). In the following paragraph, we consider the dynamic stress state shown in Fig. 8 in terms of the physical processes occurring within the cylinder.

At the start of chemical cycling ($t = 0$), the surface concentration of hydrogen is instantaneously fixed at

$c = c_{eq}$, while the rest of the cylinder is hydrogen-free. The surface of the specimen therefore experiences a large driving force to expand, but is constrained by the rest of the cylinder. Thus, the surface layers of the cylinder are loaded elastically in compression, and carry the largest stresses observed during cycling. To maintain axial force balance, the remainder of the cylinder is loaded in tension at more modest stress levels. After this initial rapid charging of the surface layers, those layers are effectively hydrogen-saturated, and do not experience additional chemical strains; the surface compressive stresses thus relax by creep, until there is essentially no stress carried by the surface layers (e.g., $t \approx 30$ s in Fig. 8). Thereafter, as the interior portions of the specimen become charged with hydrogen, a similar situation arises, in which the specimen center experiences compressive stresses, and the surface layers carry tension to meet the axial force balance. As time progresses and the entire specimen becomes saturated with hydrogen, the internal stresses (compressive in the specimen interior and tensile at the surface) decay by creep, to very low levels near the end of the half-cycle (<0.5 MPa). Upon hydrogen discharging, the events described above are essentially replayed, but with the sign of the stresses reversed, due to the shrinkage which attends the loss of hydrogen from the specimen.

In both experimental and theoretical studies of internal stress plasticity, it has often been noted that the linear flow law observed at small applied stresses breaks down as the stress is increased, and the material deforms according to a typical power-law [10, 12, 17, 18, 40, 61]. The stress range over which this transition occurs is roughly characterized by the internal stress state due to the mechanism providing internal mismatch. For example, Sherby *et al.* [10, 62, 63] derived a simple model for internal stress plasticity, which they applied to the case of anisotropic thermal expansion of Zn and U [10]. In their model,

the thermal mismatch gives rise to an internal stress, σ_i. When the applied stress is small compared to σ_i, these authors predict a linear flow law. Conversely, if the applied stress is large compared to σ_i, the model yields a deformation power-law. A similar relationship is found by Sato and Kuribayashi [40] for the case of thermal expansion mismatch between a spherical particle and the surrounding matrix, and by Mitter [64] and Schuh and Dunand [18] for the case of an allotropic phase transformation. Several numerical models have yielded similar results [5, 65, 66].

In the cases described above, the critical stress, σ_c, which defines the transition from linear to power-law behavior is the internal von Mises equivalent stress, σ_{eq}^i, averaged over the volume of the deforming phase, V, and over the duration of the cycle, Δt:

$$\sigma_c = \frac{1}{V \cdot \Delta t} \cdot \iint\limits_{\Delta t\,V} \sigma_{eq}^i \cdot dV \cdot dt \qquad (24)$$

Because the model stress state is assumed to be simply uniaxial, the internal equivalent stress, $\sigma_{eq}^i = |\sigma_i|$, where the internal chemical stress σ_i is determined in the absence of any applied stress ($\sigma = 0$). Because of the discretization of the specimen cross-section in the model, the volume integral in equation (24) is replaced with a finite sum over the $N = 100$ concentric annuli used in the computation. The time-integral in equation (24) is then computed numerically over the duration of the cycle.

Figure 9 shows the time dependence of the internal equivalent stress during hydrogen cycling with $\Delta \varepsilon = 0.11\%$, averaged over the specimen volume. It shows, in more compact form, the same evolution of stress depicted in detail in Fig. 8. The initial large stresses are due to the steep chemical gradients near the specimen surface, which relax by creep. The subsequent development of large stresses in the specimen

center gives rise to a local stress maximum near $t \approx 100$ s, and finally the global decay of internal stresses by creep is observed for the rest of the half-cycle. For comparison, the state of charging is shown on the secondary axis in Fig. 9, as given by the concentration of hydrogen at the center of the cylinder; the 12-min. half cycle time is shown sufficient to completely charge or discharge the specimen.

With the same input parameters described earlier, the critical transition stress σ_c was computed with equation (24), by numerically integrating the output of the analytical model over the cycle time (i.e., area under the curve shown in Fig. 9). When the chemical swelling strain is taken to be $\Delta \varepsilon_s = 0.08\%$ or 0.11%, the average internal chemical stress is found to be $\sigma_c = 0.83$ or 0.90 MPa, respectively. Thus, the model predicts that the transition from linear deformation behavior at low applied stresses to power-law deformation at higher applied stresses should occur in the vicinity of 0.8–0.9 MPa. Examining Fig. 6, we note that the model does appear to first deviate from linearity at $\sigma \approx 1$ MPa. Furthermore, the experimental data follow the model in this divergence, and appear to become non-linear first at a stress near 1.25 MPa. These values are in good agreement with the prediction of equation (24).

Although the model described above is quite successful in predicting the experimental data, it is useful to apply a simple criterion to determine the range of stresses over which the linear flow law is expected to be valid. Thus, in the following we describe an alternate, simpler, method of predicting the critical internal transition stress σ_c. During a complete chemical half-cycle (i.e., full charging or discharging) in the absence of applied stress, each volume element in the specimen experiences a strain equal to the swelling strain, $\Delta \varepsilon_s$, over a time of $\Delta t / 2$. Thus, the net internal strain rate is $\dot{\varepsilon} = 2 \cdot \Delta \varepsilon_s / \Delta t$. Since deformation occurs according to the power-law of equation (1), the internal stress corresponding to this average strain rate is given by:

$$\sigma_c = \left[\frac{2}{K} \cdot \frac{\Delta \varepsilon_s}{\Delta t} \right]^{\frac{1}{n}} \qquad (25)$$

This expression has a similar form to that derived by Greenwood and Johnson [12] for the case of transformation-mismatch stresses. Using the two bounds on $\Delta \varepsilon_s$ described earlier (0.08% and 0.11%), as well as the experimental values for the creep parameters K and n and the full cycle time $\Delta t = 24$ min, equation (25) gives values for the critical transition stress of $\sigma_c = 1.2 - 1.3$ MPa. These values are in good agreement with the more rigorous calculations based on equation (24) and the analytical model ($\sigma_c = 0.83 - 0.90$ MPa), as well as the approximate value obtained from the experimental data ($\sigma_c \approx 1.25$ MPa). Thus, the simple approximation of equation (25) may be used to determine the stress range over which the linear-
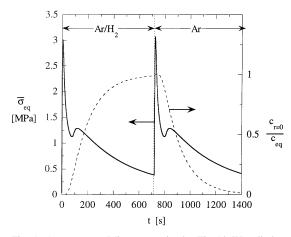

Fig. 9. Average von Mises stress in the Ti-6Al-4V cylinder during a modeled chemical cycle. The hydrogen concentration at the cylinder center (i.e., the completeness of hydrogen charging) is also shown for comparison.

and power-laws may be expected during chemical cycling.

4.5. Effect of temperature on internal stress plasticity

Internal stress plasticity has been frequently considered as a shape-forming technology, as it allows materials which are normally difficult to deform to exhibit superplastic behavior [1, 67, 68]. For thermally-induced mismatches, the effect of temperature (i.e., cycle shape, amplitude, and average temperature) on global deformation behavior is of considerable interest as a processing parameter [18, 69], and thermal inhomogeneity can lead to premature failure [70]. In the present case of chemical-swelling induced internal stress plasticity, a change in temperature leads to changes in many important material properties (i.e., elastic modulus, creep rate, hydrogen diffusivity, and equilibrium hydrogen concentration) which impact the operation of this deformation mechanism.

In this section, we briefly consider the effect of test temperature during chemical cycling of Ti-6Al-4V, by performing a parametric study with the analytical model. We consider a temperature range of 1000–1100°C (all within the β-field of Ti-6Al-4V), while maintaining a constant cycle time of 24 min, and the same half-cycle hydrogen pressures, $P = 0$ and 3.8 kPa. The temperature dependence of the elastic modulus is taken from Ref. [44] for pure β-Ti, and an Arrhenius temperature dependence (with activation energy $Q = 153$ kJ/mol for pure β-Ti [44]) is assumed for the creep parameter K. The diffusivity of hydrogen in Ti-6Al-4V is also assumed to have the same activation energy as for β-Ti, $Q = 28$ kJ/mol, from Ref. [41]. Finally, the equilibrium concentration of hydrogen on the charging half-cycle is temperature-dependent through equation (5).

The predicted strain histories during hydrogen-cycling at various temperatures are shown in Fig. 10. As expected, the heights of these curves are significantly different, primarily due to the decrease in hydrogen uptake with temperature. However, it is somewhat unexpected that the strain developed after a complete chemical cycle is virtually identical across the full range of temperatures. This lack of temperature sensitivity has several implications for possible implementation of internal stress plasticity in shape-forming applications. First, the strain evolved during a chemical cycle cannot be increased by a modest increase in temperature. This prediction is important, since lower operating temperatures are easier and less costly to sustain, lead to less contamination of the material by absorption of atmosphere-borne impurities, and induce less degradation of the processing equipment. Although hydrogen diffusion will be faster at elevated temperatures, and could lead to more rapid chemical cycles, the impact on the net strain rate will be small. Second, stringent control of thermal gradients is not necessary for chemically-induced internal stress plasticity. Although microstructural superplasticity and
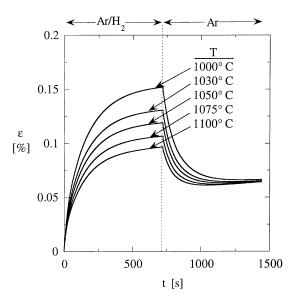

Fig. 10. Predicted hydrogen-cycling histories for Ti-6Al-4V at various temperatures in the β-phase field under an applied tensile stress of $\sigma = 0.5$ MPa.

thermal-cycling induced internal stress plasticity require thermal homogeneity to prevent necking [70], even large thermal gradients are not expected to significantly affect the strain rate during chemical cycling.

5. CONCLUSIONS

Internal stress plasticity requires the simultaneous presence of internal mismatch stresses and an external biasing stress. In the present work, we have experimentally demonstrated, for the first time, that internal stress plasticity can occur due to the presence of chemical stresses, caused in this case by dynamic concentration gradients produced by cyclic charging/discharging of β-phase Ti-6Al-4V with gaseous hydrogen. Tensile deformation experiments at 1030°C involved alternating exposure to pure argon and an argon/hydrogen mixture. The cyclic absorption and desorption of hydrogen from the metal induced chemical stresses, which were biased by the external tensile stress. The main points of this work are listed below:

- In a static atmosphere of either pure Ar or Ar/3.66% H_2, β-phase Ti-6Al-4V deforms by power-law creep with a stress exponent near three at low stresses (below about 5 MPa). Dissolved hydrogen does not significantly impact the isothermal creep behavior of the alloy.
- During chemical cycles of 24 or 30 min duration, specimens were found to deform at rates faster than by isochoral creep in a constant-composition atmosphere, particularly at stresses below about 1.5 MPa. Additionally, the average strain rate during chemical cycling was found to be proportional

to the applied stress. These two characteristics demonstrate the operation of internal stress plasticity during chemical cycling.

- A new analytical model has been developed to consider the effect of diffusion and chemical strains on uniaxial creep. The model has been applied to our experimental data using input parameters determined experimentally in this work and taken from the literature, without adjustable parameters. It predicts the strain evolution during chemical cycling with accuracy, as well as the strain developed after a complete cycle within about 15% for all of the investigated stresses.

- The average internal equivalent stress was calculated using the analytical model, and was found to accurately characterize the transition from the linear flow law observed at low stresses to a power-law at higher stresses. Also, a simple expression was developed to predict this transition point without the need for a more complex model.

REFERENCES

1. Nieh, T. G., Wadsworth, J. and Sherby, O. D., *Superplasticity in Metals and Ceramics*. Cambridge University Press, Cambridge, 1997.
2. Pickard, S. M. and Derby, B., in *9th Risø International Symposium on Metallurgy and Materials Science*, ed. S. I. Andersen, H. Lilholt and O. B. Pedersen. Risø National Laboratory, Roskilde, Denmark, 1988, p. 447.
3. Daehn, G. S. and Gonzalez-Doncel, G., *Metall. Trans.*, 1989, **20A**, 2355.
4. Daehn, G. S. and Oyama, T., *Scripta metall. mater.*, 1988, **22**, 1097.
5. Povirk, G. L., Nutt, S. R. and Needleman, A., *Scripta metall. mater.*, 1992, **26**, 461.
6. Kitazono, K. and Sato, E., *Acta mater.*, 1998, **46**, 207.
7. Kitazono, K. and Sato, E., *Acta mater.*, 1999, **47**, 135.
8. Pickard, S. M. and Derby, B., *Scripta metall. mater.*, 1991, **25**, 467.
9. Kitazono, K., Hirasaka, R., Sato, E., Kuribayashi, K. and Motegi, T., in *Superplasticity: Current Status and Future Potential*, ed. P. B. Berbon, M. Z. Berbon, T. Sakuma and T. G. Langdon. MRS, Warrendale PA, 2000, p. 199.
10. Wu, M. Y., Wadsworth, J. and Sherby, O. D., *Metall. Trans.*, 1987, **18A**, 451.
11. Lobb, R. C., Sykes, E. C. and Johnson, R. H., *Metal Sci. J.*, 1972, **6**, 33.
12. Greenwood, G. W. and Johnson, R. H., *Proc. Roy. Soc. Lond.*, 1965, **283A**, 403.
13. Clinard, F. W. and Sherby, O. D., *Acta metall.*, 1964, **12**, 911.
14. de Jong, M. and Rathenau, G. W., *Acta metall.*, 1961, **9**, 714.
15. Zwigl, P. and Dunand, D. C., *Metall. Mater. Trans.*, 1998, **29A**, 565.
16. Kot, R., Krause, G. and Weiss, V., in *The Science, Technology and Applications of Titanium*, ed. R. I. Jaffe and N. E. Promisel. Pergamon, Oxford, 1970, p. 597.
17. Schuh, C. and Dunand, D. C., *Acta mater.*, 1998, **46**, 5663.
18. Schuh, C. and Dunand, D. C., *Acta mater.*, 2001, **49**, 199.
19. Dunand, D. C. and Bedell, C. M., *Acta mater.*, 1996, **44**, 1063.
20. Zwigl, P. and Dunand, D. C., *Metall. Mater. Trans.*, 1998, **29A**, 2571.
21. Dunand, D. C. and Grabowski, J. G., *J. Am. Ceram. Soc.*, 2000, **83**, 2521.
22. Huang, C. Y. and Daehn, G. S., in *Superplasticity and Superplastic Forming 1995*, ed. A. K. Ghosh and T. R. Bieler. TMS, Warrendale, PA, 1996, p. 135.
23. Huang, C. -Y. and Daehn, G. S., *Acta mater.*, 1997, **45**, 4283.
24. Dunand, D. C., Schuh, C. and Goldsby, D. L., *Phys. Rev. Lett.*, 2001, **86**, 668.
25. Frary, M., Schuh, C. and Dunand, D. C., *Phil. Mag. A*, 2001, **81**, 197.
26. Dunand, D. C. and Zwigl, P., *Metall. Mater. Trans.*, 2001, **32A**, 841.
27. Zwigl, P. and Dunand, D. C., *J. Mater. Proc. Tech.*, in print.
28. Li, J. C. -M., *Metall. Trans.*, 1978, **9A**, 1353.
29. Lee, S. and Li, J. C. M., *J. Appl. Phys.*, 1981, **52**, 1336.
30. Chu, J. L. and Lee, S., *J. Appl. Phys.*, 1993, **73**, 2239.
31. Chu, J. -L. and Lee, S., *J. Appl. Phys.*, 1993, **73**, 3211.
32. Lee, S., Wang, W. L. and Chen, J. R., *Mater. Sci. Eng.*, 2000, **A285**, 186.
33. Szkliniarz, W. and Smolka, G., *J. Mater. Proc. Tech.*, 1995, **53**, 413.
34. ASM-Handbook, *Alloy Phase Diagrams*. ASM, Metals Park, OH, 1992.
35. Eliezer, D., Eliaz, N., Senkov, O. N. and Froes, F. H., *Mater. Sci. Eng.*, 2000, **A280**, 220.
36. Senkov, O. N. and Jonas, J. J., *Metall. Mater. Trans.*, 1996, **27A**, 1869.
37. Seshacharyulu, T., Medeiros, S. C., Morgan, J. T., Malas, J. C., Frazier, W. G. and Prasad, Y. V. R. K., *Mater. Sci. Eng.*, 2000, **A279**, 289.
38. Seshacharyulu, T., Medeiros, S. C., Morgan, J. T., Malas, J. C., Frazier, W. G. and Prasad, Y. V. R. K., *Scripta mater.*, 1999, **41**, 283.
39. Greenwood, G. W. and Johnson, R. H., *Journal of Nuclear Energy*, 1962, **16**, 473.
40. Sato, E. and Kuribayashi, K., *Acta metall. mater.*, 1993, **41**, 1759.
41. Lewcowicz, I., *Diffusion and Defect Data*, 1996, **49–50**, 239.
42. McQuillan, A. D., *Proc. Roy. Soc. Lond.*, 1950, **A204**, 309.
43. Nelson, H. G., in *Hydrogen Effects in Materials*, ed. A. W. Thompson and N. R. Moody. TMS, Warrendale, PA, 1996, p. 699.
44. Frost, H. J. and Ashby, M. F., *Deformation-Mechanism Maps: The Plasticity and Creep of Metals and Ceramics*. Pergamon Press, Oxford, 1982.
45. Adler, P. N., Schulte, R. L., Schneid, E. J., Kamykowski, E. A. and Kuehne, F. J., *Metall. Trans.*, 1980, **11A**, 1617.
46. Mahajan, Y., Nadiv, S. and Kerr, W. R., *Scripta metall.*, 1979, **13**, 695.
47. Pittinato, G. F. and Hanna, W. D., *Metall. Trans.*, 1972, **3**, 2905.
48. Derby, B., *Scripta metall.*, 1985, **19**, 703.
49. de Silva, A. R. T. and Chadwick, G. A., *J. Mech. Phys. Solids*, 1969, **17**, 387.
50. Garmong, G., *Metall. Trans.*, 1974, **5**, 2183.
51. Garmong, G., *Metall. Trans.*, 1974, **5**, 2191.
52. Garmong, G., *Metall. Trans.*, 1974, **5**, 2199.
53. Daehn, G. S., *Scripta metall. mater.*, 1989, **23**, 247.
54. Daehn, G. S. and Anderson, P. M., *Scripta metall. mater.*, 1991, **25**, 2279.
55. Dutta, I., *Acta mater.*, 2000, **48**, 1055.
56. Zhang, H., Anderson, P. M. and Daehn, G. S., *Metall. Mater. Trans.*, 1994, **25A**, 415.
57. Crank, J., *The Mathematics of Diffusion*. Oxford University Press, Oxford, 1989.
58. Schuh, C., Ph.D. Thesis, Northwestern University, 2001.
59. Senkov, O. N., DuBois, M. and Jonas, J. J., *Metall. Mater. Trans.*, 1996, **27A**, 3963.

60. Christ, H. -J., Decker, M. and Zeitler, S., *Metall. Mater. Trans.*, 2000, **31A**, 1507.
61. Zwigl, P. and Dunand, D. C., *Acta mater.*, 1997, **45**, 5285.
62. Sherby, O. D. and Wadsworth, J., *Advances and Future Directions in Superplastic Materials*, in *Superplasticity*. 1989, NATO Report AGARD-LS-168. p. 3.1.
63. Sherby, O. D. and Wadsworth, J., *Mat. Sci. Technol.*, 1985, **1**, 925.
64. Mitter, W., *Umwandlungsplastizität und ihre Berücksichtigung bei der Berechnung von Eigenspannungen.* 1987, Gebr. Bornträger: Berlin. p. 40.
65. Zhang, H., Daehn, G. S. and Wagoner, R. H., *Scripta metall. mater.*, 1991, **25**, 2285.
66. Zwigl, P. and Dunand, D. C., in *German-Austrian ABAQUS User Conference*, Innsbruck University, 1997, p. 75.
67. Chen, Y. C., Daehn, G. S. and Wagoner, R. H., *Scripta metall. mater.*, 1990, **24**, 2157.
68. Dunand, D. C. and Myojin, S., *Mater. Sci. Eng.*, 1997, **230A**, 25.
69. Kitazono, K., Sato, E. and Kuribayashi, K., *Acta mater.*, 1999, **47**, 1653.
70. Schuh, C. and Dunand, D. C., *J. Mater. Res.*, 2001, **16**, 865.

APPENDIX A

In this appendix we show how the system of N equations, with N unknowns $\dot{\sigma}_i$, described by equation (15) can be solved analytically. First, the coefficient matrix is bidiagonalized by eliminating all of the terms but the first in the upper row. This is accomplished by adding the Nth row, twice the N-1st row, thrice the N-2nd row, etc., to the first row. Thus, each row, numbered j, is added to the first row $(N + 1 - j)$ times, giving:

$$
\begin{bmatrix}
N & 0 & 0 & \dots & 0 \\
1 & -1 & 0 & \dots & 0 \\
0 & 1 & -1 & \dots & 0 \\
\vdots & \vdots & \vdots & \ddots & \vdots \\
0 & 0 & 0 & 1 & -1
\end{bmatrix}
\begin{bmatrix}
\dot{\sigma}_1 \\
\dot{\sigma}_2 \\
\dot{\sigma}_3 \\
\vdots \\
\dot{\sigma}_N
\end{bmatrix} \qquad (A1)
$$

$$
= E \cdot
\begin{bmatrix}
\sum_{j=2}^{N} b_j \cdot (N + 1 - j) \\
b_2 \\
b_3 \\
\vdots \\
b_N
\end{bmatrix}
$$

or, dividing the first row by N and the remaining rows by -1,

$$
\begin{bmatrix}
1 & 0 & 0 & \dots & 0 \\
-1 & 1 & 0 & \dots & 0 \\
0 & -1 & 1 & \dots & 0 \\
\vdots & \vdots & \vdots & \ddots & \vdots \\
0 & 0 & 0 & -1 & 1
\end{bmatrix}
\begin{bmatrix}
\dot{\sigma}_1 \\
\dot{\sigma}_2 \\
\dot{\sigma}_3 \\
\vdots \\
\dot{\sigma}_N
\end{bmatrix} = E \cdot
\begin{bmatrix}
S \\
-b_2 \\
-b_3 \\
\vdots \\
-b_N
\end{bmatrix} \qquad (A2)
$$

in which

$$
S = \frac{1}{N} \cdot \sum_{j=2}^{N} b_j \cdot (N + 1 - j) \qquad (A3)
$$

Equation (A2) can now be solved for $\dot{\sigma}_i$ as follows. First, the upper row is added to the second row. The resulting second row is added to the third row, the subsequent third row is added to the fourth, as so on, until the matrix is reduced to the identity matrix, I. The solution of the system of equations (equation (15)) is then found as:

$$
\begin{bmatrix}
\dot{\sigma}_1 \\
\dot{\sigma}_2 \\
\dot{\sigma}_3 \\
\vdots \\
\dot{\sigma}_N
\end{bmatrix} = E \cdot
\begin{bmatrix}
S \\
S - b_2 \\
S - b_2 - b_3 \\
\vdots \\
S - \sum_{k=2}^{N} b_k
\end{bmatrix} \qquad (A4)
$$

Thus, the instantaneous rate of stress change can be computed from knowledge of the stress state, elastic and creep constitutive behavior, and a description of the chemical swelling behavior of the material.